Dispersion engineering by hybridizing the back-folded soft mode

# of monomode elastic metamaterials with stiff acoustic modes

Michael F. Groß, Jonathan L.G. Schneider, Yi Chen*, Muamer Kadic, and Martin Wegener*

M.F. Groß, Y. Chen, M. Wegener

Institute of Nanotechnology, Karlsruhe Institute of Technology (KIT), Karlsruhe 76128, Germany.

M.F. Groß, J.L.G. Schneider, Y. Chen, and M. Wegener

Institute of Applied Physics, Karlsruhe Institute of Technology (KIT), Karlsruhe 76128, Germany.

M. Kadic

Université de Franche-Comté, Institut FEMTO-ST, UMR 6174, CNRS, Besançon 25000, France.

E-mail: yi.chen@partner.kit.edu (Y.C.); martin.wegener@kit.edu (M.W.)

Keywords: dispersion engineering, roton-like bands, monomode elastic metamaterials, mode hybridization, back-folded modes, soft modes

Abstract:

In many cases, the hybridization of two or more excitation modes in solids has led to new and useful dispersion relations of waves. Well-studied examples are phonon polaritons, plasmon polaritons, particle-plasmon polaritons, cavity polaritons, and magnetic resonances at optical frequencies. In all of these cases, the lowest propagating mode couples to a finite-frequency localized resonance. Herein, the unusual metamaterial phonon dispersion relations arising from the hybridization of an ordinary acoustical phonon mode with a back-folded soft or easy phonon mode of a monomode elastic metamaterial are discussed. Conceptually, the single easy mode can have strictly zero wave velocity. In reality, its wave velocity is very much smaller than that of all other modes. Considering polymeric 3D printed elastic monomode metamaterials at ultrasound frequencies, it is shown theoretically and experimentally that the resulting pronounced avoided crossing, with a frequency splitting comparable to the mid-frequency, leads to backward-wave behavior for the lowest band over a broad frequency range, conceptually at zero loss.

1. Introduction

Coupling of two identical harmonic oscillators with eigenfrequency $\omega_1 = \omega_2$ via coupling strength K (with unit s^{-1}) leads to two different eigenmodes and eigenfrequencies $\omega_1 \pm K$ of the coupled system.[1] This situation is often referred to as an avoided crossing or, in terms of quantum chemistry, as a hybridization. Coupling between a harmonic-oscillator-type resonance with frequency $\omega_2 = \mathrm{const.}$ and a propagating mode with dispersion relation starting as $\omega_1(k) = v_1\, k$, with wavenumber k and wave speed v_1, also leads to a famous avoided crossing known as the polariton dispersion relation.[2, 3] A scheme is shown in **Figure 1**(a). The dashed black curves are the uncoupled modes, and the solid red curves illustrate the coupled or hybridized modes. For example, in metals, coupling of the plasmon at frequency $\omega_2(k) = \omega_{\mathrm{pl}}$ and the dispersion relation of light $\omega_1(k) = ck$ leads to a surface-wave dispersion relation with a flat region with small group velocity that allows for very large k, equivalent to nanometer wavelengths $\lambda = 2\pi/k$, at optical frequencies – which has attracted considerable scientific interest in plasmonics.[4-6]

Numerous further types of avoided crossing have been discussed in the literature.[7, 8] Recently, hybridization of different photon modes[9] or phonon[11-18] modes has been exploited to realize dispersion relations resembling the roton dispersion relation of sound in liquid Helium-4.[19] This dispersion relation contains a broad region of backward waves, for which group velocity and phase velocity have opposite sign, indicating a negative refractive index.[20, 21] However, achieving these hybridizations required sophisticated three-dimensional (3D) metamaterial architectures providing strong and complex nonlocal beyond-nearest-neighbor interactions[11] or extreme chiral couplings.[22, 23]

Here, we consider a much simpler approach based on the coupling of an ordinary propagating acoustical phonon mode starting as $\omega_1(k) = v_1 k$ for small wavenumbers k and a back-folded soft mode $\omega_2(k)$ of a monomode metamaterial. $\omega_1(k)$ and $\omega_2(k)$ are shown by the two dotted black curves in Figure 1(b). In extremal Cauchy-elastic metamaterials,[24-33] an integer N of the six (three) eigenmodes in three dimensions (two dimensions) are soft or "easy". For monomode metamaterials, we have $N = 1$. Introducing a strong coupling between the two dotted black curves leads to the hybridized bands shown as solid red curves in Figure 1(b). The lower of them exhibits a roton-like behavior.[10] We note that extremal pentamode ($N = 5$)[34-38] and tetramode ($N = 4$)[39-41] 3D metamaterials have recently attracted considerable attention. In contrast, monomode ($N = 1$) metamaterials have been studied less so far. Notable exceptions are, for example, Miura-ori metamaterials.[42,43] We also note that back-foldings have been extensively exploited to achieve double Dirac cones in topological insulators, leading to pseudo spin-Hall effects in optical, acoustical, and mechanical systems.[44-46]

Here, we strongly couple the two mentioned branches (black dotted curves in Figure 1(b)) by introducing a superlattice with a period $N_x\, a$ (with integer $N_x \geq 2$) along the x-direction larger than the monomode metamaterial period a or by a finite lateral extent $N_x\, a$ of a monomode metamaterial beam. This coupling leads to the red curves shown in Figure 1(b). We also consider dissecting a bulk monomode metamaterial into a superlattice of separated metamaterial beams of width $N_x\, a$ (or into just a single such beam). Our corresponding finite-element calculations of the resulting hybridized band structure $\omega_i(k)$ $(i = 1,2, \dots)$ are in good agreement with optical-microscopy and Doppler-vibrometry based ultrasound measurements of this elastic band structure for polymeric monomode-metamaterial beam samples manufactured by three-dimensional (3D) laser microprinting.

2. Metamaterial design

Our design approach starts from a bulk monomode elastic metamaterial composed of a 2D periodic lattice of extruded rhombuses, as illustrated in **Figure 2**(a). The shown unit cell, highlighted by the black square, leads to a metamaterial in-plane period or lattice constant a. Note that the corresponding unit cell is not the primitive Wigner-Seitz cell. The Wigner-Seitz cell, enclosed by the dashed lines, is smaller in real space, hence the corresponding Brillouin zone is larger than ours. The choice of the unit cell does not change the physics. We choose the unit cell shown in Figure 2(a) for clarity. The extrusion length a_z along the z-direction (cf. Figure 2(a)) is irrelevant as long one considers a 3D periodic structure. Below, we will also consider slab geometries, in which case a_z becomes the thickness of the slab or perforated plate. The extruded rhombuses in the unit cell are connected at their corners by thin elements with characteristic thickness d, which represents the critical parameter of the structure. In the limit of $d/a \to 0$, these connections approximate ideal joints. Such joints have

previously been used in extremal metamaterials based on rotating squares or double-cone structures.[47-53] They enable easy or soft modes, in the present case a single soft mode.

This soft mode becomes apparent when plotting the calculated eigenfrequencies for the shear-wave branch shown in **Figure 3**(a) (the used finite-element approach is described in Methods). Here, we consider a bulk monomode metamaterial, i.e., we consider an infinite periodic lattice along all three spatial directions, using the unit cell as defined in Figure 2(a). The geometrical parameters (cf. Figure 2) as well as the Young's modulus E, Poisson's ratio ν, and mass density ρ of the constituent polymer material to be used in our below experiments are given in the caption of Figure 2. In Figure 3(a), the soft mode shows up as a minimum or groove of the dispersion relation along the diagonal within the $k_x k_y$-plane. The soft mode can be physically interpreted as a shear deformation along the diagonals of the monomode metamaterial, since the small connecting parts between the rhombuses can hardly resist bending. In the limit of an ideal monomode metamaterial, this groove would lie at strictly zero frequency, $\omega = 0$. Furthermore, the monomode feature of the metamaterial can directly be identified from the six eigenvalues, i.e., 3.295 GPa, 0.875 GPa, 0.385 GPa, 0.296 GPa, 0.296 GPa, and 0.006 GPa, of the effective elastic matrix obtained from the phase velocities in the long-wavelength limit.[41] One of the six eigenvalues (the last one) is about three orders of magnitude smaller than the other five eigenvalues, as expected for a monomode metamaterial.[24] If one now considers an in-plane supercell with period $N_x\, a$, for example with integer $N_x = 3$, the frequency surface is back-folded. More specifically, the green part and the red part (cf. Figure 3(a)) on the frequency surface are shifted by $2\pi/(N_x a)$ along the negative k_x-direction, and the black dashed curve in between the green and red parts is back-folded to $k_x = 0$. The dashed black curves in Figure 1(b) correspond to the same conditions as in Figure 3(a) with $N_x = 3$. The eigenstates and eigenfrequencies are still the same as those of the original not-backfolded system, they are merely represented differently.

However, once we introduce a coupling between the two uncoupled branches, the situation changes. There are several possibilities to achieve such coupling. First, we can change the structure shown in Figure 2(a) such that its periodicity actually becomes that of the supercell. This situation is illustrated in Figure 2(b). Here, we have added material hence mass (see dark blue regions) with periodicity $N_x\, a$, again for the example $N_x = 3$. The resulting, albeit initially weak, hybridization of the bands (cf. the small gap between the two red curves) can be seen in Figure 3(b). The uncoupled bands are also plotted here as dashed lines for comparison. The lowest red band exhibits an obvious roton-like minimum at a wavenumber $k_y = 2\pi/(N_x a)$, related to the back-folded soft shear mode. In previous theoretical work on laminate materials, similar roton-like behaviors have been observed, yet they required compressional prestress or much more complicated geometries.[54, 55] Additionally, as illustrated in Figure 2(c), we can disconnect parts of the structure such that the bulk monomode metamaterial turns into an array of disconnected beams. In this case, the physics of one metamaterial beam and its dispersion relation is the same as that of an array of beams (apart from the multiple degeneracy for multiple beams). As this truncation in Figure 2(c) is a yet stronger perturbation to the

system than the situation in Figure 2(b), we expect a yet stronger coupling between the previously uncoupled branches, which can be inferred from the much larger bandgap between the lowest red branch and higher bands shown in Figure 3(c). Notably, not only does the back-folding and hybridization of the bands survive the transition from a bulk to a beam geometry, the effect of this perturbation also extends to other bands. For $N_x = 3$, the second lowest band, corresponding to longitudinal modes in the bulk case, shows a pronounced roton-like behavior with even two regions of negative slope. The number of these regions is determined by the number of unit cells along the width of the beam, in the sense that a larger N_x gives rise to additional regions with $\mathrm{d}\omega/\mathrm{d}k < 0$. To illustrate this dependence, we exhibit further calculations for bulk metamaterials and metamaterial beam with $N_x = 2$ and $N_x = 3$ in the Supporting Information (Figure S2 and Figure S4). We explain the roton-like dispersion of the longitudinal band by strong admixture with the transverse modes, for which the back-folding and hybridization has already been discussed above. This admixture becomes more evident when comparing the displacement-vector field of a longitudinal mode within a bulk metamaterial ($N_x = N_y = \infty$) to that of a metamaterial beam ($N_x = 3, N_y = \infty$). In the bulk case, the longitudinal mode exhibits a displacement-vector field which is mostly parallel to the phonon wave vector. In the beam case, however, large displacement components orthogonal to the wave vector arise, which are generally rather attributed to transverse modes. Therefore, it is fair to treat the formerly longitudinal modes as now mixed, or one might say longitudinal-like modes, which are influenced by the same back-folding and hybridization mechanism we have discussed above for the transverse modes. To summarize the design, we have seen that the two critical parameters that determine the dispersion relation are the connection width d and the back-folding parameter N_x.

Moving on to the experiments, in which we study the influence of both of these parameters, the degeneracy of the dispersion relation for multiple beams means that it is sufficient to investigate a single beam of finite width $N_x\, a$. All above phonon bands are calculated by using 2D planar metamaterial structures that are infinitely large along the z-direction. The same band hybridizations also occur in a three-dimensional metamaterial beam with a finite out-of-plane extrusion length $a_z = 600\ \mu\mathrm{m}$ (Figure S4, Supporting Information). However, as for any beam, an out-of-plane shear mode and a twist mode occur additionally. These bands somewhat complicate the band structure.

We note in passing that the metamaterial-beam dispersion relations $\omega_1(k)$ of the lowest band could be expanded into a Taylor series according to $\omega_1^2(k) = a_2k^2 + a_4k^4 + a_6k^6 \ldots$. Translated from reciprocal space into real space, this expansion leads to a phenomenological effective-medium description containing higher-order spatial gradients – in perfect analogy to the discussion in Ref.[11]. However, to capture the metamaterial-beam dispersion relation quantitatively, rather high orders are required, which may limit the practicability of such effective-medium description.

3. Experimental results and discussion

Example optical micrographs of such finite metamaterial beam samples, which we have fabricated using a commercial laser printer (Photonics Professional GT, Nanoscribe) and a commercial photoresist (IP-S, Nanoscribe), are depicted in **Figure 4**(a). We have realized beam samples with either a supercell size of $N_x = 2$ or $N_x = 3$. A different number of local minima and maxima in the dispersion relation of the lowest acoustic band of the phonon band structure are clearly visible. Band structure calculations as in Figure 3(c), but for $N_x = 2$ are shown in Figure S2 and Figure S4 of the Supporting Information. The targeted geometrical parameter values are: $a = 300\ \mu\text{m}, a_z = 600\ \mu\text{m}, d = 16.4\ \mu\text{m}$ and $D = 148.5\ \mu\text{m}$ (cf. Figure 2(a)), leading to the critical parameter ratio $d/a = 0.055$. Each metamaterial beam contains $N_y = 40$ unit cells along the beam axis (= y-axis).

In order to obtain the phonon band structure for the lowest acoustic bands experimentally, we have excited the metamaterial beam samples by a piezoelectric transducer assembly as shown in Figure 4(b). The main axis of the transducer is aligned with the metamaterial beam axis. Therefore, the transducer mainly induces elastic waves with a displacement vector oriented along the y-axis. We improve the coupling of the mechanical excitation to the eigenmodes of the sample by filling out some of the voids in the transition region between the periodic metamaterial beam and the bottom plate underneath it. This results in a wedge-shaped polymer structure (cf. Figure 4(a)) which effectively serves as a termination of the sample and matches the excitation displacement to the displacement-vector field of the modes of the lowest bands. Without such transition region, it can happen that certain modes are hardly excited at all and, hence, do not appear in the band-structure measurements.

In these experiments, the sample is imaged from the side using a home-built laser-scanning confocal back-scattering microscope, while the transducer is driven with a time-harmonic voltage of variable frequency $f = \omega/(2\pi)$. For each frequency, we extract the in-plane displacement-vector components $u_x(\mathbf{r}, t)$ and $u_y(\mathbf{r}, t)$ from these image data using digital image cross-correlation (DIC) analysis. Simultaneously, we record the third, namely the out-of-plane, component of the displacement vector, $u_z(\mathbf{r}, t)$, by laser-Doppler vibrometry. Both techniques allow for the time-resolved mapping of the displacement-vector field with nanometer-scale localization errors.[23, 41] In this work, typical displacement amplitudes are roughly in the range of $2 - 40\ \text{nm}$ (depending on frequency and component of the displacement vector). The band structure is derived from these data by Fourier transformation with respect to time t and with respect to coordinate vector $\mathbf{r}$. It is sufficient

to restrict the displacement-vector measurements to the real space-coordinates that follow the lattice periodicity, hence to the $\mathbf{r}_j = (0, ja, 0)^{\mathrm{T}}$ with $j \in [0, N_y]$. To improve image contrast and hence the signal-to-noise ratio in the DIC analysis, we have introduced small cross-shaped or cylindrical markers on the sample surface (cf. Figure 4(a)). We provide more details in the Methods section and the Supporting Information. The two-dimensional Fourier transformation of $\mathbf{u}(\mathbf{r}, t)$ yields the complex-valued response function $\tilde{A}(k_y, \omega)$, the modulus of which we plot to visualize our experimental results. In **Figure 5**, we depict $|\tilde{A}(k_y, \omega)|$ as a false-color plot, where the dispersion relation of the phonon bands can be recognized by following the maxima. For comparison, the dispersion relation is overlaid by solid lines, which represent the calculated band structure of an infinitely long beam (i.e., $N_y = \infty$).

Figure 5(a) presents the measured dispersion relation for a sample with $N_x = 2$ unit cells along the x-axis, i.e., the supercell size is $2a$. The three panels show the dispersion relations calculated from the individual displacement-vector components (from left to right) $u_x(\mathbf{r}, t)$, $u_y(\mathbf{r}, t)$ and $u_z(\mathbf{r}, t)$.

The roton-like bands in Figure 5(a) appear when detecting the components $u_x(\mathbf{r}, t)$ and $u_y(\mathbf{r}, t)$. This finding can be explained by the fact that the corresponding modes do not have a "pure" displacement-vector field polarization along either the x- or the y-direction. Rather do the corresponding modes each feature nonzero displacement-vector field components along both, the x- and the y-axis. Therefore, the Fourier transforms of both, $u_x(\mathbf{r}, t)$ and $u_y(\mathbf{r}, t)$, reveal the corresponding bands. This behavior is distinct from the flexural band of the beam, whose displacement-vector field is mainly oriented along the z-axis, hence out-of-plane. The rightmost panel in Figure 5(a) completes the dataset by showing the corresponding dispersion relation derived by Fourier transformations of $u_z(\mathbf{r}, t)$. Only a single prominent band, the ordinary flexural band of a beam or plate is detected. The bands with roton-like dispersion are absent here, since the corresponding modes feature no significantly large displacement-vector components along the z-axis.

4. Conclusion

Since the birth of the idea of metamaterials early on this Century, different approaches to tailor the dispersion relation of waves in metamaterials have been established. This includes mainly exploiting Bragg reflections and coupling to local resonances, but also using chirality (broken space-inversion symmetry), broken time-inversion symmetry, and nonlocal (beyond nearest-neighbor) interactions. Here, we have suggested theoretically and realized experimentally a yet different approach, namely the hybridization of ordinary acoustical phonons and backfolded soft phonon modes in monomode-metamaterial beams. By tailoring a critical small geometrical parameter and the number of unit cells in the width of the metamaterial beam (which determines the level of back-folding), we have achieved one or more maxima as well as minima in the dispersion relations of the lowest acoustical-phonon bands within the first Brillouin zone. Working with the lowest band provides broadband and robust behavior. Such behavior is achieved here by geometrically much simpler metamaterial architectures than previously along other lines of design. Specifically, we here present an effectively two-dimensional structure, which is extruded into the third dimension. In essence, this geometry corresponds to a perforated plate. Such architecture is much simpler than a truly three-dimensional structure with lots of overhanging parts during a 3D print process (cf. [11] and [23]). As a result, the present structure is amenable for manufacturing by many different means, including simply machining of a plate. We have used 3D printing here to allow for a direct comparison with previous work. Measured and calculated band structures are in excellent overall agreement. This work based on monomode metamaterials may stimulate further work on other less well explored extremal Cauchy elastic metamaterials, such as dimode and trimode metamaterials.

5. Methods

Band Structure Computation: The phonon dispersion relations of the designed metamaterial are obtained by using the commercial software COMSOL Multiphysics and its Solid Mechanics Module. We solve the following eigenfrequency problem for linear elastic wave propagation

$$\frac{E}{2(1+v)(1-2v)}\nabla\left(\nabla\cdot\mathbf{u}_{\mathbf{k},n}(\boldsymbol{r})\right)+\frac{E}{2(1+v)}\nabla^2\mathbf{u}_{\boldsymbol{k},n}\,(\mathbf{r})=-\rho\omega_{\mathbf{k},n}^2\,\mathbf{u}_{\mathbf{k},n}\,(\mathbf{r}). \qquad (1)$$

Here, $\omega_{\mathbf{k},n}$ represents the eigenfrequency with the band index n, $\mathbf{k}$ is the Bloch wave vector, and $\mathbf{u}_{\mathbf{k},n}\,(\mathbf{r})$ is the displacement-vector field of the corresponding eigenmode. For wave propagation in

bulk metamaterials (c.f. Figure 3(b), Figure S1, Supporting Information), Bloch-periodic boundary conditions are applied along both the x- and the y-directions. For wave propagation in metamaterial beams (c.f. Figure 3(c), Figure S2 and Figure S4, Supporting Information), Bloch-periodic boundary conditions are only applied along the y-direction. Other boundaries are set to be the default traction free boundaries in the Solid Mechanics Module. For the constituent polymer resulting from the 3D laser microprinting, we choose the parameters of $E = 4.19\ \mathrm{GPa}$ for the Young's modulus, $\nu = 0.4$ for the Poisson's ratio, and $\rho = 1140\ \mathrm{kg\ m^{-3}}$ for the mass density.[41]

Monomode Beam Sample Fabrication: A commercially available 3D laser microprinter (Photonics Professional GT, Nanoscribe) was used for the fabrication of the metamaterial beam samples. The printing was performed with a 25× objective lens of numerical aperture $\mathrm{NA} = 0.8$ (Carl Zeiss) in dip-in mode using a liquid photo resist (IP-S, Nanoscribe). The samples with a critical parameter of $d = 16.4\ \mu\mathrm{m}$ and $d = 45.2\ \mu\mathrm{m}$ were printed with a laser power of $50\ \mathrm{mW}$, while the samples with $d = 9.3\ \mu\mathrm{m}$ were printed with a significantly reduced laser power of $20\ \mathrm{mW}$. All powers were measured at the entrance pupil of the objective lens. For each value of d, samples with $N_x = 2$ and $N_x = 3$ were fabricated. All samples featured $N_y = 40$ unit cells along the y-axis, resulting in a total height of $12\ \mathrm{mm}$. A hatching distance of $500\ \mathrm{nm}$ and slicing distance of $1.5\ \mu\mathrm{m}$ together with a scanning focus velocity of $0.14\ \mathrm{ms^{-1}}$ were chosen for the printing of all samples shown in this paper. The metamaterial beams were printed in one piece together with a bottom plate (cf. Figure 4(a)) featuring a small handle to ease sample manipulation when gluing the samples onto a piezoelectric transducer. To remove residual unpolymerized photoresist after printing, the samples were submerged for 45 minutes in a bath of propylene glycol monomethyl ether acetate (PGMEA), followed by a 5 minutes rinsing in acetone. Finally, the samples were dried under ambient laboratory conditions. The numerical model for the material geometry and the bottom plate were designed in the commercial software COMSOL Multiphysics. Additional details on the sample geometry are included as STL-files and on the fabrication as machine code (GWL-files) for the laser printer within the data repository published together with this work (to be added).

Experiment Setup and Ultrasound Single-Frequency Excitation: The 3D-tracking of elastic waves within the metamaterial beam samples was conducted by using a home-built confocal optical back-scattering microscope with an integrated Mach-Zehnder type heterodyne laser-Doppler vibrometry branch, following the methods of previous publications on mechanical microscale metamaterials.[23,

[41] The metamaterial-beam sample under investigation was glued onto a piezoelectric transducer (PL055.31 PICMA, Physik Instrumente) and positioned in the focal plane of the microscope objective lens (Plan L 50×/0.60, Leitz Wetzlar).

By driving the transducer with an amplified sinusoidal voltage, elastic waves were excited within the beam sample. The displacement-vector field $\mathbf{u}(\mathbf{r},t) = (u_x(\mathbf{r},t), u_y(\mathbf{r},t), u_z(\mathbf{r},t))^{\mathrm{T}}$ induced by these waves was sampled sequentially along 41 regions of interest (ROI) along the beam y-axis. The spacing of the ROIs follows the lattice periodicity a with $\mathbf{r}_j = (0, ja, 0)^{\mathrm{T}}$ with integer $j \in [0, N_y]$. We centered each ROI on either a cross-shaped marker on a rhomboid or on a circular-shaped marker (cf. Figure 4(a)) for tracking by the DIC analysis. All samples investigated contained a total of 16 cross-shaped markers per unit cell, all samples except for one additionally contained one circular-shaped marker per unit cell. The presented results have been obtained by choosing only one marker per unit cell. This has led to sufficient signal-to-noise ratio already. As band structures derived from measurements on different markers are conceptually equivalent, taking data on different markers would allow for further improving the signal-to-noise ratio. The data shown in Figure 5(a) have been obtained using one of the cross-shaped markers. The data of all other Figures have been obtained using the circular marker. In Figure 4, the used ROI are indicated by the red squares. To position each ROI in the focal plane of the objective lens, three piezo-inertia translation stages (Q-545, Physik Instrumente) were used. Recovery of the temporal phase information of the displacement data was guaranteed by synchronizing the data acquisition of the confocal microscopy and the Doppler vibrometry to the transducer drive signal. Every sample was investigated at each ROI over a frequency interval from $10\ \mathrm{kHz}$ to $600\ \mathrm{kHz}$ in steps of $5\ \mathrm{kHz}$, to cover the frequency range of the back-folded and hybridized bands. Subsequently, the in-plane displacement components $u_x(\mathbf{r},t)$ and $u_y(\mathbf{r},t)$ were extracted from the raw data by performing digital image cross-correlation analysis on the images acquired with the confocal microscope. The out-of-plane component $u_z(\mathbf{r},t)$ was supplemented by the laser-Doppler vibrometry signal data to which a standard in-phase and quadrature demodulation technique was applied.[56]

Supporting Information

The Supporting Information is available from the Wiley Online Library or from the author.

Acknowledgements

M.G., J.S., and Y.C. contributed equally to this work. This research has been funded by the Deutsche Forschungsgemeinschaft (DFG, German Research Foundation) under Germany's Excellence Strategy via the Excellence Cluster "3D Matter Made to Order" (EXC-2082/1-390761711), by the Carl Zeiss Foundation through the "Carl-Zeiss-Foundation-Focus@HEiKA", and by the Helmholtz program "Materials Systems Engineering" (MSE). M.K. is grateful for support by the ANR PNanoBot (ANR-21-CE33-0015) and ANR OPTOBOTS project (ANR-21-CE33-0003).

Conflict of interests

Authors declare that they have no competing interests.

Data and code availability

The data that support the plots within this paper. Other findings of this study are available from the corresponding authors upon reasonable request and are published on the open access data repository of the Karlsruhe Institute of Technology [to be added].

References

[1] C. Kittel, *Introduction to solid state physics*, Wiley, New York **2005**.

[2] W. A. Murray, W. L. Barnes, *Adv. Mater.* **2007**, *19*, 3771.

[3] V. M. Agranovich, V. Ginzburg, *Crystal optics with spatial dispersion, and excitons*, Springer, Heidelberg **2013**.

[4] A. Alù, N. Engheta, *Phys. Rev. E* **2005**, *72*, 16623.

[5] N. Engheta, R. W. Ziolkowski, *Metamaterials: physics and engineering explorations*, Wiley, **2006**.

[6] F. Monticone, A. Alu, *Rep. Prog. Phys.* **2017**, *80*, 36401.

[7] L. Brillouin, *Wave propagation in periodic structures*, Dover publications, New York **1953**.

[8] B. R. Mace, E. Manconi, *J. Acoust. Soc. Am.* **2012**, *131*, 1015.

[9] Y. Chen, M. A. A. Abouelatta, K. Wang, M. Kadic, M. Wegener, *Adv. Mater.* **2023**, 2209988.

[10] Y. Chen, M. Kadic, M. Wegener, *Nat. Commun.* **2021**, *12*, 3278.

[11] J. A. I. Martínez, M. F. Groß, Y. Chen, T. Frenzel, V. Laude, M. Kadic, M. Wegener, *Sci. Adv.* **2021**, *7*, eabm2189.

[12] Q. Wu, P. Shivashankar, X. Xu, Y. Chen, G. Huang, *J. Compos. Mater.* **2022**, 40562.

[13] Z. Zhu, Z. Gao, G. Liu, Y. Ge, Y. Wang, X. Xi, B. Yan, F. Chen, P. P. Shum, H. Sun, Y. Yang, *New J. Phys.* **2022**, *24*, 123019.

[14] K. Wang, Y. Chen, M. Kadic, C. Wang, M. Wegener, *Commun. Mat.* **2022**, *3*, 35.

[15] J. Cui, T. Yang, M. Niu, L. Chen, *J. Appl. Mech.* **2022**, *89*, 111005.

[16] G. J. Chaplain, I. R. Hooper, A. P. Hibbins, T. A. Starkey, *Phys. Rev. Appl.* **2023**, *19*, 44061.

[17] K. Wang, Y. Chen, M. Kadic, C. Wang, M. Wegener, *Acta Mech. Sin.* **2023**, *39*, 723020.

[18] Y. Chen, K. Wang, M. Kadic, S. Guenneau, C. Wang, M. Wegener, *Commun. Phys.* **2023**, *6*, 1.

[19] H. Godfrin, K. Beauvois, A. Sultan, E. Krotscheck, J. Dawidowski, B. Fåk, J. Ollivier, *Phys. Rev. B* **2021**, *103*, 104516.

[20] C. M. Soukoulis, M. Kafesaki, E. N. Economou, *Adv. Mater.* **2006**, *18*, 1941.

[21] V. M. Shalaev, *Nat. Photon.* **2007**, *1*, 41.

[22] J. Kishine, A. S. Ovchinnikov, A. A. Tereshchenko, *Phys. Rev. Lett.* **2020**, *125*, 245302.

[23] Y. Chen, J. L. G. Schneider, M. F. Groß, K. Wang, S. Kalt, P. Scott, M. Kadic, M. Wegener, *Adv. Funct. Mater.* **2023**.

[24] G. W. Milton, A. V. Cherkaev, *J. Eng. Mater. Technol.* **1995**, *117*, 483.

[25] M. Kadic, T. Bückmann, N. Stenger, M. Thiel, M. Wegener, *Appl. Phys. Lett.* **2012**, *100*, 191901.

[26] C. N. Layman, C. J. Naify, T. P. Martin, D. C. Calvo, G. J. Orris, *Phys. Rev. Lett.* **2013**, *111*, 24302.

[27] Y. Tian, Q. Wei, Y. Cheng, Z. Xu, X. J. Liu, *Appl. Phys. Lett.* **2015**, *107*, 221906.

[28] X. Su, A. N. Norris, C. W. Cushing, M. R. Haberman, P. S. Wilson, *J. Acoust. Soc. Am.* **2017**, *141*, 4408.

[29] Y. Chen, M. Zheng, X. Liu, Y. Bi, Z. Sun, P. Xiang, J. Yang, G. Hu, *Phys. Rev. B* **2017**, *95*, 180104.

[30] Z. Sun, H. Jia, Y. Chen, Z. Wang, J. Yang, *J. Acoust. Soc. Am.* **2018**, *3*, 1029.

[31] H. Dong, S. Zhao, X. Miao, C. Shen, X. Zhang, Z. Zhao, C. Zhang, Y. Wang, L. Cheng, *J. Mech. Phys. Solids* **2021**, *152*, 104407.

[32] Z. Hu, Z. Wei, K. Wang, Y. Chen, R. Zhu, G. Huang, G. Hu, *Nat. Commun*. **2023**, *14*, 1266.

[33] R. V. Craster, S. R. Guenneau, K. Muamer, M. Wegener, *Rep. Prog. Phys.* **2023**, *Accepted*.

[34] N. Norris, *Pro. R. Soc. A* **2008**, *464*, 2411.

[35] T. Bückmann, M. Thiel, M. Kadic, R. Schittny, M. Wegener, *Nat. Commun.* **2014**, *5*, 1.

[36] M. Kadic, T. Bückmann, R. Schittny, P. Gumbsch, M. Wegener, *Phys. Rev. Appl.* **2014**, *2*, 54007.

[37] F. Fraternali, A. Amendola, *J. Mech. Phys. Solids* **2017**, *99*, 259.

[38] Y. Chen, B. Zhao, X. Liu, G. Hu, *Extreme Mech. Lett.* **2020**, *40*, 100916.

[39] Y. Wei, X. Liu, G. Hu, *Mater. Des.* **2021**, *210*, 110031.
[40] Y. Wei, G. Hu, *Extreme Mech. Lett.* **2022**, *55*, 101789.
[41] M. F. Groß, J. L. G. Schneider, Y. Wei, Y. Chen, S. Kalt, M. Kadic, X. Liu, G. Hu, M. Wegener, *Adv. Mater.* **2023**, 2211801.
[42] Y. Chen, R. Peng, Z. You, *Science* **2015**, *349*, 396-400.
[43] M. Schenk, S. D. Guest, Proc. Natl. Acad. Sci. U.S.A. **2013**, *110*, 3276-3281.
[44] L. H. Wu, X. Hu, *Phys. Rev. Lett.* **2015**, *114*, 223901.
[45] C. He, X. Ni, H. Ge, X. Sun, Y. Chen, M. Lu, X. Liu, Y. Chen, *Nat. Phys.* **2016**, *12*, 1124.
[46] Y. Chen, X. Liu, G. Hu, *J. Mech. Phys. Solids* **2019**, *122*, 54.
[47] T. Bueckmann, R. Schittny, M. Thiel, M. Kadic, G. W. Milton, M. Wegener, *New J. Phys.* **2014**, *16*, 33032.
[48] Y. Cho, J. H. Shin, A. Costa, T. A. Kim, V. Kunin, J. Li, S. Y. Lee, S. Yang, H. N. Han, I. S. Choi, D. J. Srolovitz, *Proc. Natl. Acad. Sci. USA* **2014**, *111*, 17390.
[49] Y. Chen, X. N. Liu, G. K. Hu, *Sci. Rep.-UK* **2015**, *5*, 15745.
[50] R. Gatt, L. Mizzi, J. I. Azzopardi, K. M. Azzopardi, D. Attard, A. Casha, J. Briffa, J. N. Grima, *Sci. Rep.-UK* **2015**, *5*, 8395.
[51] Y. Tang, G. Lin, L. Han, S. Qiu, S. Yang, J. Yin, *Adv. Mater.* **2015**, *27*, 7181.
[52] Y. Chen, G. Hu, *Phy. Rev. Appl.* **2019**, *12*, 044046.
[53] K. K. Dudek, R. Gatt, M. R. Dudek, J. N. Grima, *Materials* **2021**, *14*, 758.
[54] K. K. Dudek, L. Mizzi, J. I. Martínez, A. Spaggiari, G. Ulliac, R. Gatt, J. N. Grima, V. Laude, M. Kadic, *Compos. Struct.* **2023**, *319*, 117151.
[55] N. Arora, Q. Yao, S. Rudykh, *Extreme Mech. Lett.* **2022**, *51*, 101592.
[56] C. Rembe, L. Mignanelli, *Laser Doppler Vibrometry for Non-Contact Diagnostics* **2020**, 9.

Figures and Captions

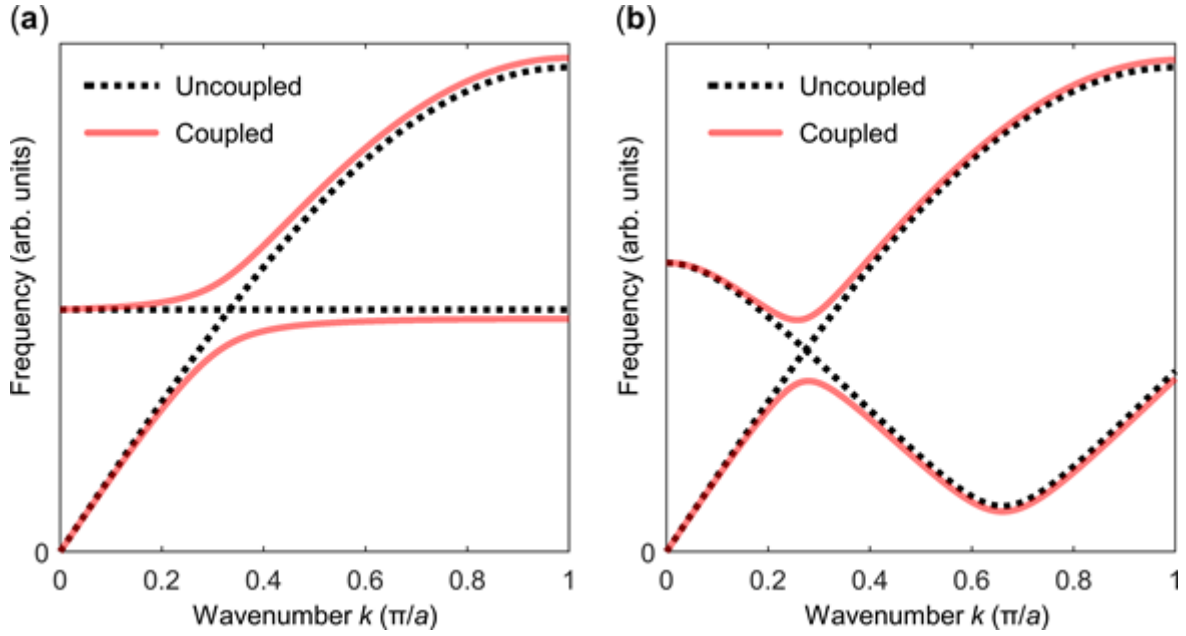

Figure 1. Illustration of dispersion engineering by band coupling. (a) Two coupled bands (red solid lines) result from hybridization between a monotonically increasing dispersive band and a flat local resonance (dashed lines). (b) The same as in (a), but for the coupling between a similar monotonically increasing band and a back-folded band of a monomode metamaterial. The coupled lowest band (red) exhibits a roton-like minimum at a finite wavenumber $k = 0.65\,\pi/a$, related to the soft shear mode of the monomode metamaterial.

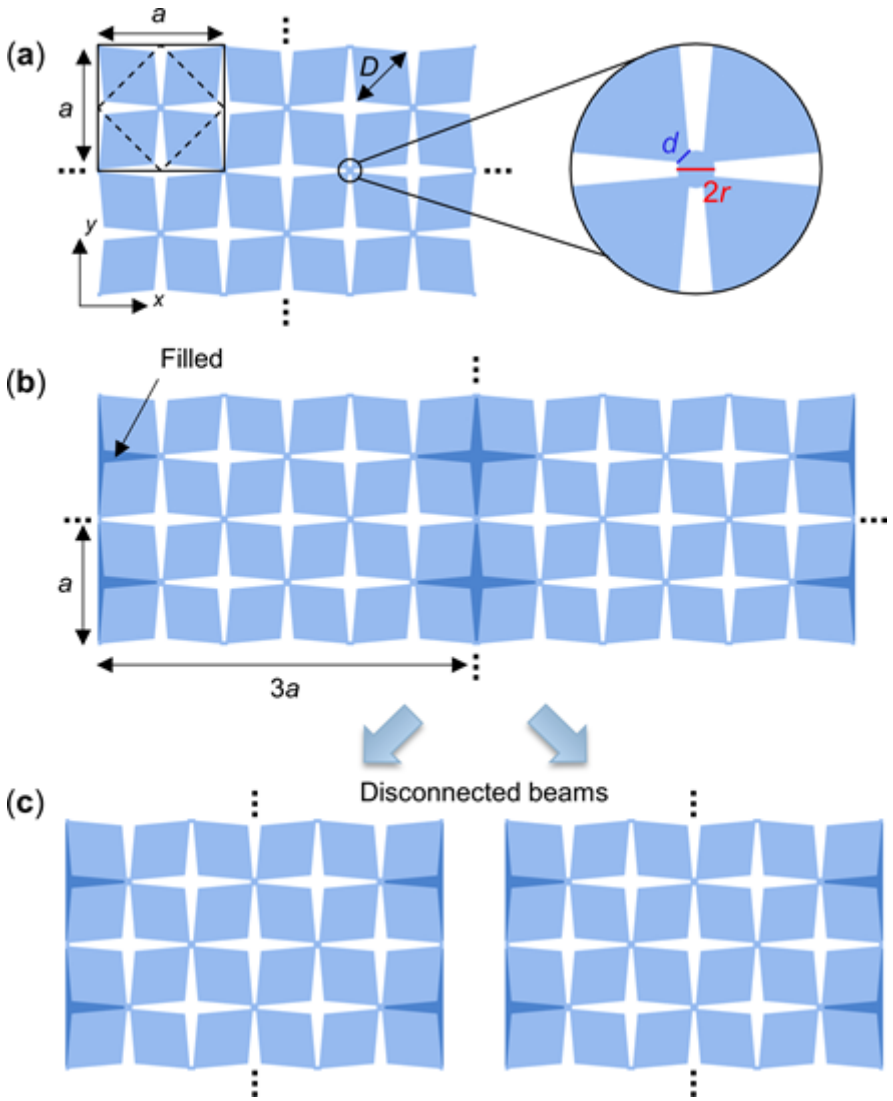

Figure 2. Design based on a monomode elastic metamaterial and a back-folding strategy. (a) A finite block of monomode metamaterial composed of rhombuses and circles (light blue). A three-dimensional metamaterial is obtained by extruding the planar structure into the out-of-plane direction. The solid black square indicates a unit cell with lattice constant a. The primitive cell corresponds to the region highlighted by the dashed square. The inset defines and emphasizes the critical parameter d. For sufficiently small values of d/a, the metamaterial approaches an ideal monomode elastic material. The corresponding "easy" or soft mode is a shear mode. Its wavevector is oriented along the diagonal of the monomode metamaterial.
(b) A supercell metamaterial is obtained by adding fillings (dark blue) into the void at a period of $3a$ along the x-direction. The larger period of $3a$ along the x-direction leads to a smaller first Brillouin zone compared to the metamaterial in (a), and thereby induces back-folded bands. Colors are for illustration only. All parts correspond to the same laser

printed polymer, for which we assume the Young's modulus $E = 4.19\ \mathrm{GPa}$, the Poisson's ratio $v = 0.4$, and the mass density $\rho = 1190\ \mathrm{kg\ m^{-3}}$ in the numerical calculations. (c) By cutting apart the metamaterial in (b) at a period of $3a$ along the x-direction, we obtain metamaterial beams with a finite lateral size but with a conserved period of a along the y-direction. A simple perspective sketch of the metamaterial beam is depicted in Figure S3. Compared to phonon bands of the bulk metamaterial in (a), the phonon bands of the metamaterial beam are dramatically altered by this lateral boundary condition.

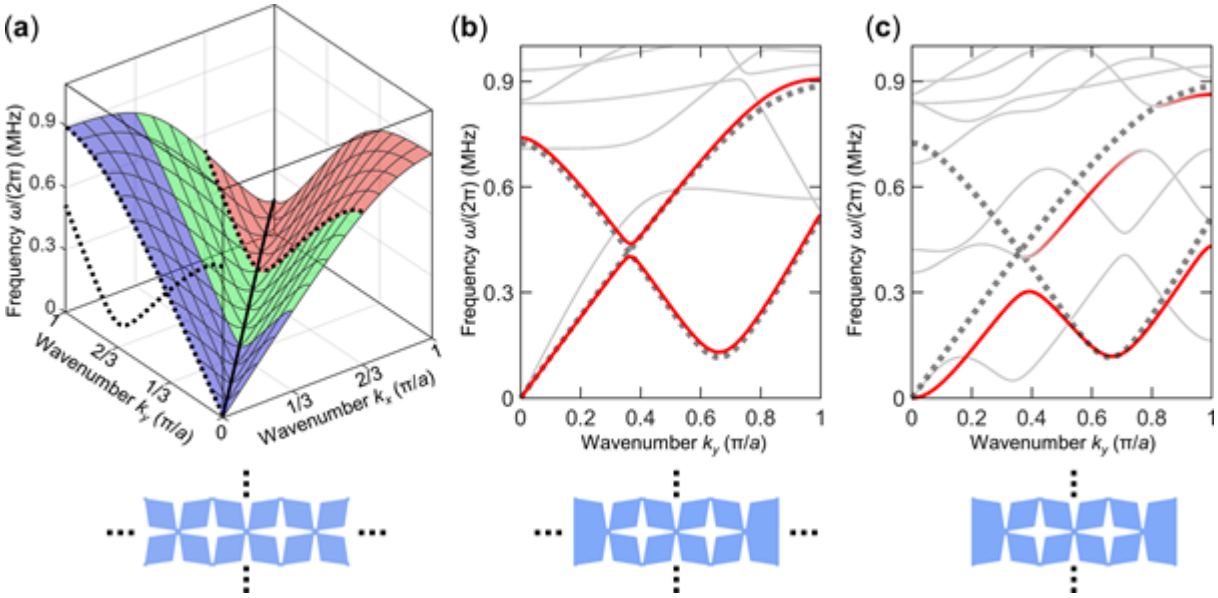

Figure 3. Dispersion surface and dispersion bands of designed metamaterials. (a) Plot of the lowest eigenfrequency $\omega/(2\pi)$ versus the wavenumber k_x and k_y for the designed monomode metamaterial in Figure 2(a). The lowest eigenfrequency corresponds to a shear mode in the metamaterial. Frequencies along the diagonal direction (c.f. the black line) are much smaller, reflecting the soft shear mode in the metamaterial. For illustration, the frequency surface is divided into three colored parts. Considering a virtual supercell with a period of $3a$ along the x-direction, the dispersion surface will be back-folded into a smaller Brillouin zone with the wavenumber range of $-\pi/(3a) < k_x < \pi/(3a)$. The green and the red parts will be translated by a distance of $2\pi/(3a)$ along the negative k_x-direction, and the black dashed curve in between the green and red parts will be shifted to $k_x = 0$. The two dashed curves at the plane of $k_x = 0$ are similar to the two uncoupled bands as in Figure 1. (b) Two coupled bands (red lines) are obtained by adding filling to the supercell geometry as demonstrated in Figure 2. The two uncoupled bands are re-plotted as dashed gray curves for comparison. (c) The same as in (b), but for a metamaterial beam with finite size along the x-direction. Due to a strong influence of the boundaries to the phonon bands, the coupled red bands belong to multiple bands. The geometry parameters $D/a = 0.5$, $r/a = 0.05$, $d/a = 0.04$, and the lattice constant $a = 300\ \mu\mathrm{m}$ are chosen here. The Supplementary Movie S1 shows the eigenmode for (a) and

wavevector $\boldsymbol{k = \pi/a(\frac{2}{3}, \frac{2}{3})}$. Supplementary Movie S2 shows the eigenmode for (c) and wavenumber $\boldsymbol{k_y = 0.5\,\pi/a}$.

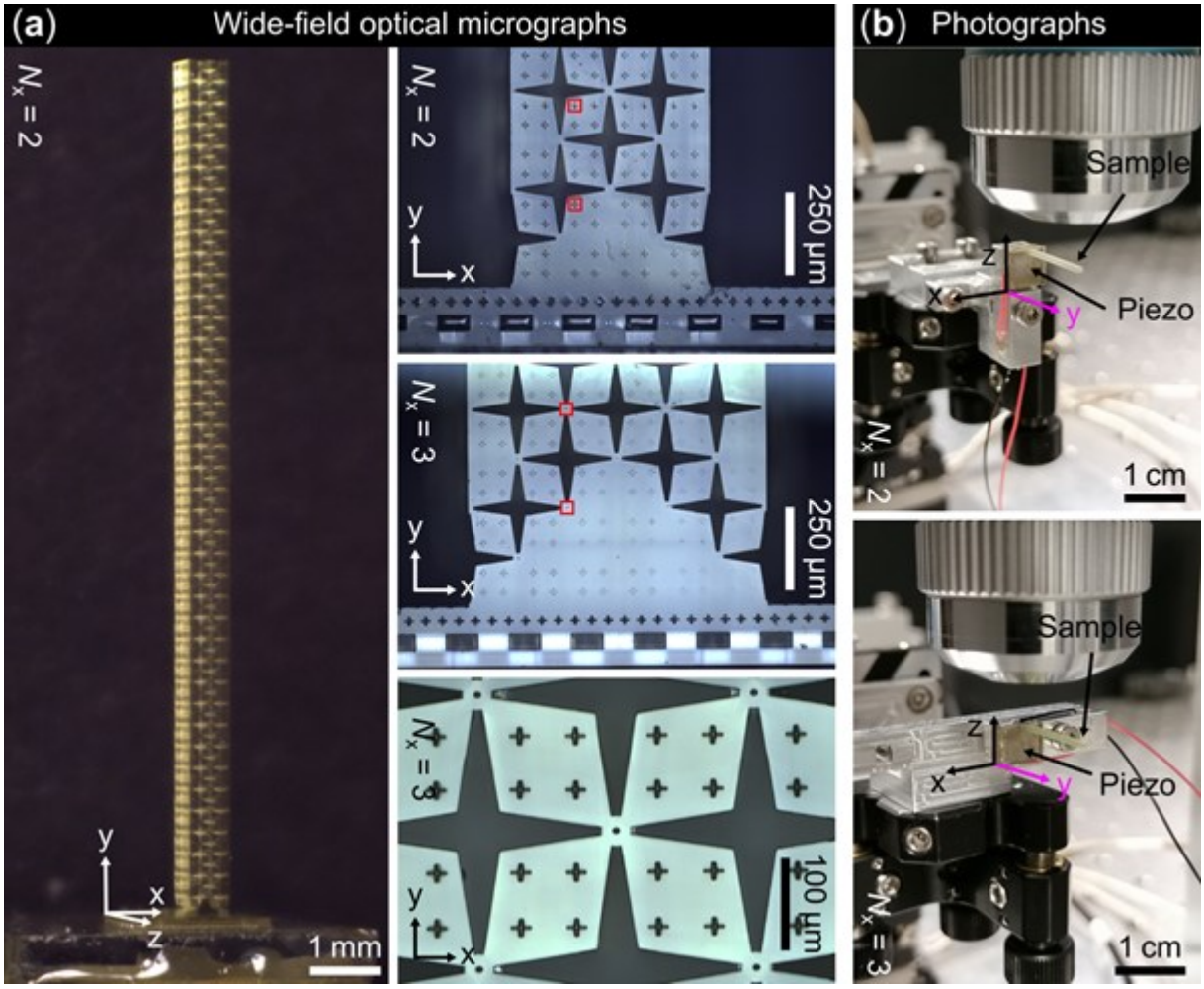

Figure 4. Gallery of monomode metamaterial beam samples. (a) Wide-field optical micrographs of several sample features. On the left, an overview of a metamaterial beam with $N_y = 40$ layers along the beam y-axis and $N_x = 2$ unit cells is shown, yielding a total height of 12 mm. The sample was printed together with a bottom plate which can be seen close to the tripod. The pictures in the right column of (a) show close-ups of two beam samples with $N_x = 2$ (top) and $N_x = 3$ (middle) where they are connected to the bottom plate below, respectively. The latter exceeds the field-of-view and extends out of the picture horizontally. On the left and right edges of the samples, the added mass can be seen, which would introduce the periodicity of a supercell in the bulk case. The polymer structure forming a wedge where the metamaterial beam is connected to the bottom plate acts as a termination to efficiently excite the desired eigenmodes of the

metamaterial in the experiment. Furthermore, a close-up of a single unit cell is shown on the bottom right of (a). The crosses on the rhombuses and the circular intrusions in the cylindrical hinges act as markers for tracking using digital image cross-correlation analysis to sample the displacement field $\mathbf{u}(\mathrm{r}, t)$ along the beam y-axis. The red squares indicate the used regions of interest (ROI). (b) Photographs of two samples glued onto piezoelectric-transducer assemblies for the excitation of elastic waves. The assemblies are mounted in the experimental microscopy setup of which the microscope objective lens can be seen at the top, respectively. The main piezoelectric-transducer axis is highlighted in pink in the corresponding tripods.

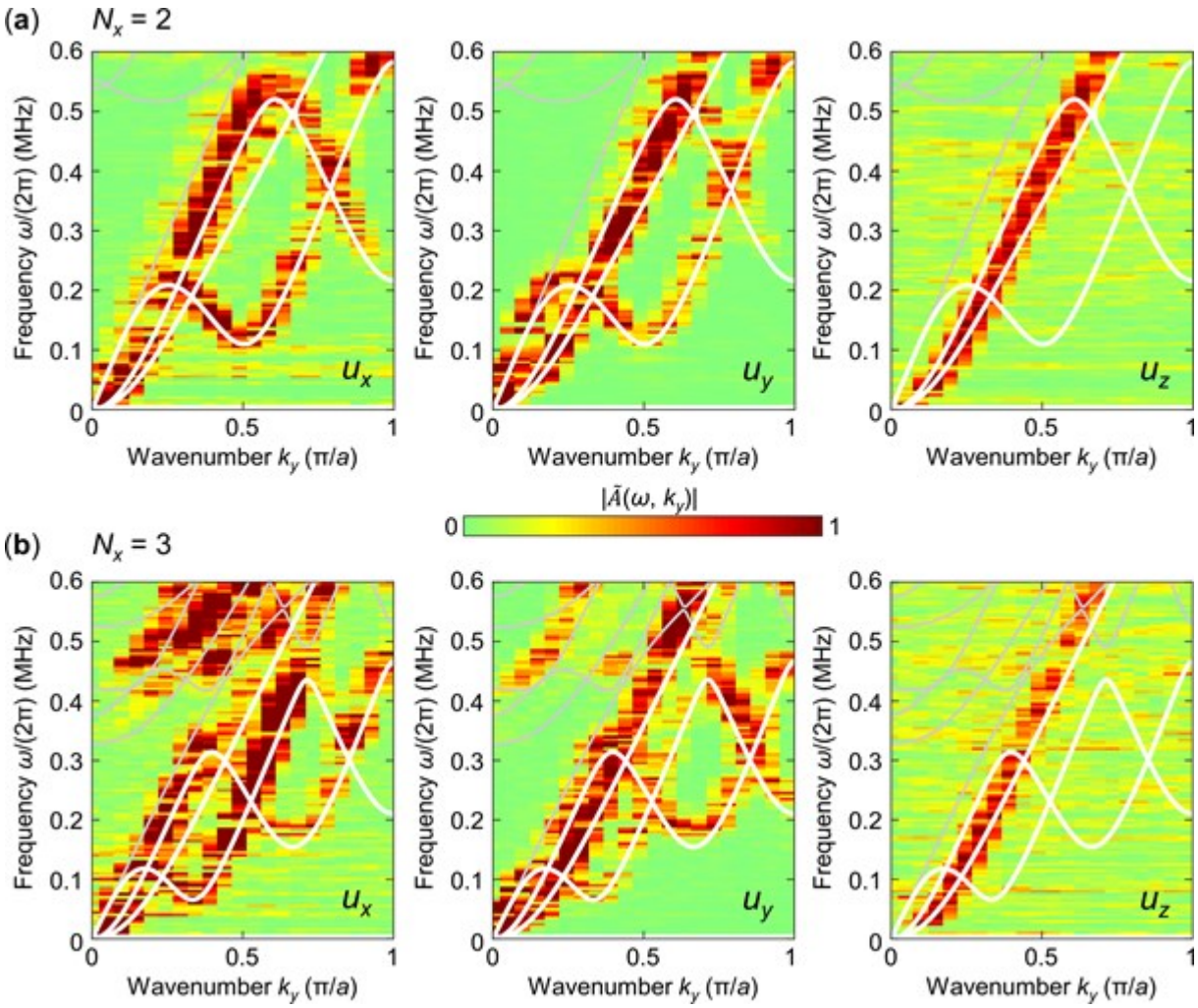

Figure 5. Measured band structures of the metamaterial beam samples with critical parameter $d = 16.4\ \mu\mathrm{m}$. The modulus of the complex response function $|A(k_y, \omega)|$ is plotted on a false-color scale versus the y-component of the wave vector and angular frequency ω, for a sample with $N_y = 40$ unit cells along the beam axis. The solid lines

represent the numerical computation results for an infinite ($N_y = \infty$) metamaterial beam, where the white lines correspond to the three lowest bands and the gray lines include higher bands for the sake of integrity. (a) Results for a sample with $N_x = 2$ unit cells along the x-axis (cf. Figure 3(a)). The three plots show the respective amplitude $|A(k_y, \omega)|$ as derived via a 2D Fourier transformation from the (left to right) x-, y- and z-component of the displacement vector field $\mathbf{u}(\mathbf{r}, t) = (u_x(\mathbf{r}, t), u_y(\mathbf{r}, t), u_z(\mathbf{r}, t))^{\mathrm{T}}$, sampled along the beam axis. The x- and y-components were extracted using optical-image digital cross-correlation analysis while the z-component was measured by the means of laser-Doppler vibrometry. In both plots derived from u_x and u_y, the roton-like band can be clearly seen. They are in good agreement with theory (white lines). The third plot shows only one band corresponding to modes polarized along the z-axis, which does not exhibit a roton-like behavior but rather the usual dispersion relation of a beam. The residual small mismatch between the slope of the calculated band and the experimental data is attributed to an underestimated Young's modulus of the constituent polymer in our simulations. (b) Similar to (a) but for a beam with $N_x = 3$, hence showing additional local maxima and minima. The excited optical modes at frequencies above $420\ \mathrm{kHz}$ are also in good agreement with the calculated bands (grey lines).

Table of Contents (ToC)

The strong coupling between ordinary phonon modes and a back-folded soft phonon mode of a monomode metamaterial is suggested as a means to engineer the metamaterial dispersion relation of the lowest bands. The back-folding is accomplished by a superlattice or a set of separated beams. Unusual roton-like phonon bands serve as an example. Calculations and experiments are in excellent agreement.

ToC figure